On the Rapid Spectral Evolution of Steep Wave Groups: Directional Spreading and the Spectral Tail

D. Barratt*[1], H.B. Bingham[2], P.H. Taylor[1,3], T.S. van den Bremer[1], T.A.A. Adcock[1]

[1]Department of Engineering Science, University of Oxford, Oxford OX1 3PJ, United Kingdom
[2]Department of Mechanical Engineering, Technical University of Denmark (DTU), 2800 Lyngby, Denmark
[3]Faculty of Engineering and Mathematical Sciences, University of Western Australia, Crawley WA 6009, Australia
*Corresponding author — E-mail: dylan.barratt@eng.ox.ac.uk

I. Introduction

Several studies have shown that wave fields which are 'out of equilibrium' can give rise to exaggerated nonlinearity due to enhanced wave-wave interactions [1–3]. Previous studies have also shown that nonlinear wave-wave interactions can alter the characteristics of an extreme wave event in the context of a random sea [4–6] as well as an isolated wave group [7–8]. In this study, we have performed numerical simulations of steep three-dimensional wave groups, formed by the dispersive focusing, using the fully-nonlinear potential flow solver *OceanWave3D*. We consider the influence of directional spreading and the high-wavenumber tail of the spectrum on the nonlinear wave-wave interactions. We perform simulations based on Gaussian as well as JONSWAP omnidirectional spectra, combined with both frequency dependent and independent spreading functions. Our simulations indicate that the localised nonlinear features of an individual steep wave event, including group shape and kinematics, may also depend on the spectral equilibrium of the initial sea-state. We conclude that focused wave events in sea-states with low directional spreading or sea-states without a fully-developed spectral tail are more likely to exhibit attributes of nonlinearity.

II. Numerical Simulations

OceanWave3D numerically solves the governing equations of potential flow for surface gravity waves with the nonlinear free-surface boundary conditions [9]. A numerical wave-tank 7.68 km in length (L), 2.56 km in width (W) and 112 m in depth (d) has been employed. The simulated wave groups have a characteristic wavelength (λ_0) of 225 m and characteristic wave period (T_0) of 12 s—based on the initial peak of the wavenumber spectrum (k_p). The water is approximated as 'deep' with $k_p d = 3.142$ and a symmetry plane has been implemented along the centreline of the wave group. We combine eighth-order finite differencing in space with classic fourth-order Runge–Kutta time marching. A detailed assessment of simulation fidelity has been previously performed [10] which informs our selection of the discretization parameters, listed in Table I. We perform simulations based on JONSWAP as well as Gaussian spectra and use a finer grid resolution for the JONSWAP cases to resolve the tail components. Simulations have been performed both excluding and including the nonlinear terms in the free-surface boundary conditions, to highlight the influence of wave-wave interactions. All boundary conditions have been calculated at the mean water level ($z = 0$) for the linear simulations. The initial conditions have been calculated for 15 characteristic wave periods before the time of linear focus ($t/T_0 = -15$), using the linear dispersion relation, and time-marched for 30 wave periods. We apply exact second-order corrections to the initial conditions based on Dalzell [11] and an approximate form of third-order correction [10]. The variance density spectrum, $F(k, \theta)$, has been implemented as the product of an omnidirectional spectrum $S(k)$ and a spreading function $D(\theta)$. Two types of omnidirectional spectrum have been considered, a Gaussian spectrum and a JONSWAP spectrum with $\gamma = 3.3$. The spectral peak is located at $k_p = 0.02796$ m^{-1} for both the Gaussian and JONSWAP spectra and a bandwidth of $k_w = 0.004606$ m^{-1} has been used for all the Gaussian cases. Note that a Gaussian spectrum represents a close approximation to the peak of a JONSWAP spectrum with $\gamma = 3.3$. Thus, we contrast our simulations of Gaussian and JONSWAP spectra to investigate the significance of the spectral tail. Two different spreading functions have been implemented: a frequency-independent Gaussian spreading function and the frequency-dependent spreading function of Ewans [12]. The spreading parameter of the Gaussian (ς_0) has been varied between 5° and 25° in increments of 5°. Following the theory of quasi-determinism [13], the scaled autocorrelation function has been used to calculate the surface elevation of the wave group, $\eta(x, y, t)$:

$$\eta(x, y, t) = A_L \frac{\sum_i F(k_i, \theta_i) \cos\left(k_i \cos\theta_i \, x + k_i \sin\theta_i \, y - \omega_i t + \varphi_0\right)}{\sum_i F(k_i, \theta_i)}. \tag{1}$$

Here, k_i is the magnitude of the wavenumber for each component, θ_i is the direction of propagation, A_L is the linear amplitude of the wave group at focus ($t/T_0 = 0$) and the angular frequency of each component (ω_i) is calculated from the arbitrary-depth linear dispersion relationship, $\omega_i = \sqrt{g k_i \tanh\left(k_i d\right)}$, based on the gravitational constant (g) and the depth of the domain (d). The phase offset (φ_0) is defined relative to a 0° baseline and additional values of 90°, 180° and 270° have been simulated for linearisation of the wave spectrum [10]. The scaled autocorrelation function is

TABLE I
Discretization Parameters.

Grid	N_x	N_y	N_z	Δx	Δy	Δt
Gaussian	1024	256	8	7.5 m	10 m	0.2s
JONSWAP	2048	512	8	3.75 m	5 m	0.2s

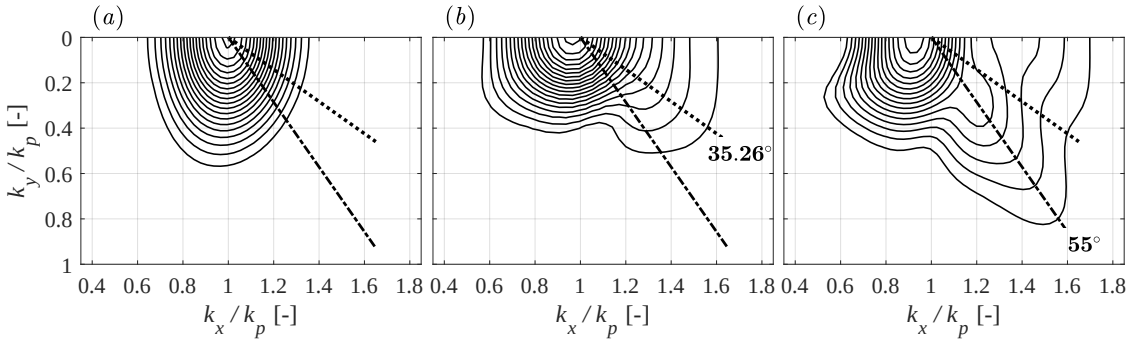

Fig. 1. Amplitude spectra of surface elevation for case GG15 with a steepness of $A_L k_p = 0.30$: (a) initial condition, $t/T_0 = -15$; (b) nonlinear focus, $t/T_0 = 1.3$; (c) post-focus, $t/T_0 = 15$. Contour levels are evenly distributed between 0.01 m and 0.0105 m in intervals of 0.005 m.

known to represent the average shape of the largest waves in a linear sea, as described by Boccotti [13], and has thus been used in this study as a model for a steep wave group.

III. Directional Energy Transfers Due to Third-Order Interactions

The wave spectrum has been calculated with a Discrete Fourier Transform (DFT) of the surface elevation, extracted at every time step from the simulations and linearised using four-phase separation [10]. We base our analysis in this section on a wave group comprised of a Gaussian omnidirectional spectrum and a Gaussian spreading function with an initial spreading parameter (ς_0) of 15° (the case is denoted as GG15) with a linear steepness of $A_L k_p = 0.30$. Figure 1 depicts contour plots of the linearised amplitude spectrum in wavenumber space for: the initial condition, $t/T_0 = -15$; the time of nonlinear focus, $t/T_0 = 1.3$; and the end of the simulation, $t/T_0 = 15$. The initial condition in Fig. 1(a) is narrow-banded and remains narrow-banded during the early stages of focusing due to the low-steepness of the initially dispersed wave group. However, evolution of the amplitude spectrum due to wave-wave interactions occurs as the wave group steepens and approaches focus. In particular, energy transfer to high-wavenumber components is evident in Fig. 1(b), with a directional-bias at angles of $\pm 35.26°$ to the spectral peak, accompanied by unidirectional energy transfers along the k_x-axis. As a consequence of wave-wave interactions, a high-wavenumber sidelobe forms and the amplitude spectrum at nonlinear focus also exhibits a contraction of the spectrum along the k_y-direction, which implies lateral expansion of the wave group and reduced directional spreading at focus. After nonlinear focus, Fig. 1(c), the amplitude spectrum continues to broaden with directional energy transfer to high-wavenumber components at a $\pm 55°$ angle. Qualitatively similar results have been observed by Adcock and Taylor [7] using the Modified Nonlinear Schrödinger equation. Thus, all spectral changes can be attributed to resonant third-order interactions, since the MNLS equation is only capable of resolving third-order/four-wave interactions as shown by Stiassnie [14].

IV. Augmented Kinematics Due to Spectral Evolution

Energy transfers to higher wavenumbers are associated with augmented kinematics since the velocities of the wave field scale with the angular frequencies of the wave components. Furthermore, the reduction in directional spreading, which occurs during focusing, increases the in-line velocity component. Figure 2 shows the surface elevation at focus for the linear, Fig. 2(a), and nonlinear, Fig. 2(b), version of the event—lateral expansion and reduced directional spreading are apparent for the nonlinear event. Assuming drag-dominant loading, force on a vertical surface-piercing column can be estimated with the drag term of the Morison equation:

$$F_D = \int_{-d}^{\eta} \frac{1}{2} C_D \rho A u(z)|u(z)|\, dz. \tag{2}$$

Here, $u(z)$ represents the horizontal velocity which varies in the vertical, z-direction. The constant C_D depends on geometry, Reynolds number and the frontal area of the body (A) as well as the density of the fluid (ρ). The total force acting on a bottom-mounted, surface-piercing structure is given by integration in the z-direction from depth d to the surface elevation η. The integral in Eq. (2) has been evaluated at the (x,y) location where focus occurs, and a time history of the force at this spatial location plotted in Fig. 2(c) for both the linear and nonlinear scenarios of case GG15 with a steepness of $A_L k_p = 0.30$. As expected, linear focus occurs at $t/T_0 = 0$ at the spatial location: $x/\lambda_0 = 0$, $y/\lambda_0 = 0$. However, the competing effects of nonlinearity and dispersion cause the nonlinear event to focus later $t/T_0 = 1.3$ at the spatial location: $x/\lambda_0 = 1.535$, $y/\lambda_0 = 0$. Separate axes have been used in Fig. 2(c) for the linear and nonlinear cases for clarity. The maximum drag of the nonlinear scenario is 24% higher than the linear scenario, as a result of energy transfers to higher wavenumbers and the reduced spreading of the nonlinear focused event.

	GG5	GG10	GG15	GG20	GG25	JG15	JE
Ave. N_i	21.16	20.18	19.70	19.35	19.09	19.84	18.54
Max N_i	25	21	21	21	21	29	27

TABLE II

Average and maximum number of GMRES iterations per time step for cases shown in Fig. 3(*b*).

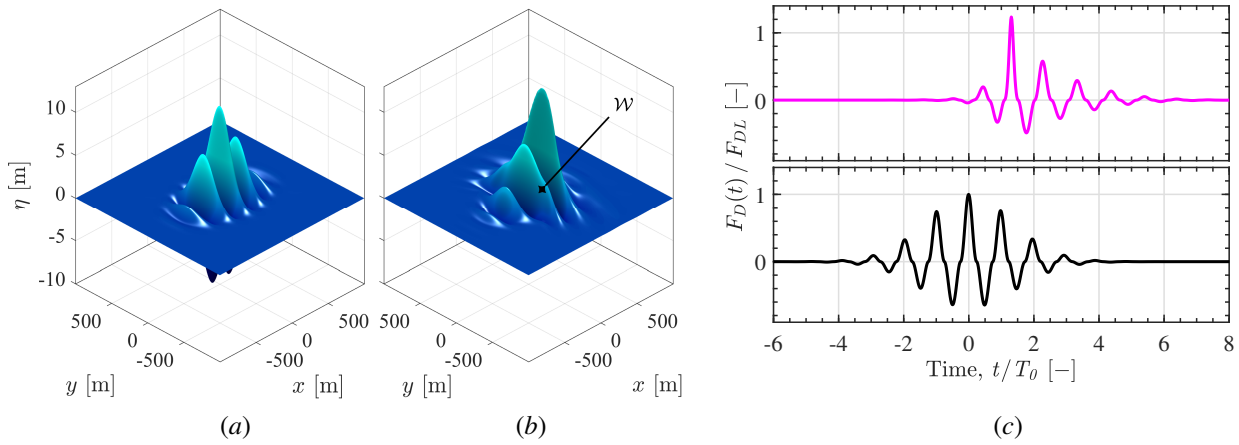

Fig. 2. Comparison of linear and nonlinear evolution for case GG15 with a steepness of $A_L k_p = 0.30$: (*a*) Surface elevation at the time of focus, $t/T_0 = 0.0$, for the linear version of the event; (*b*) Surface elevation at the time of focus, $t/T_0 = 1.3$, for the nonlinear version of the event. The formation of 'wing waves', localised regions of elevation due to energised oblique components, is demarcated with $\mathcal{W}$; (*c*) Time-history of force calculated from the drag term of the Morison equation, normalised by the maximum drag force of the linear case F_{DL}. The linear case is depicted by the black line (—) and the nonlinear case is depicted by the magenta line (—). The time-history of force is calculated at the spatial location where focus of the wave group occurs: $x/\lambda_0 = 0$, $y/\lambda_0 = 0$ for the linear case and $x/\lambda_0 = 1.535$, $y/\lambda_0 = 0$ for the nonlinear case.

V. Stabilising Effect of Spreading and the High-Wavenumber Tail

The Gaussian function represents an analytically attractive option for modelling wave spectra and the peak of the JONSWAP spectrum contains the vast majority of the total energy. Gaussian omnidirectional spectra are frequently used in studies of wave-wave interactions and the high-wavenumber components of the spectral tail neglected from the analysis. Thus, a comparison between Gaussian and JONSWAP spectra serves two purposes: (1) to indicate the appropriacy of a Gaussian spectrum as a model for the peak of a JONSWAP spectrum in general and; (2) to contrast the spectral evolution of a steep wave event in seas with and without a fully-developed spectral tail. We combine a JONSWAP omnidirectional spectrum ($\gamma = 3.3$) and a Gaussian spreading function with an initial spreading parameter of $\varsigma_0 = 15°$, and denote this case as JG15. Similarly, we combine a JONSWAP omnidirectional spectrum with the frequency dependent spreading function of Ewans [12] and denote this case as JE. We compare against two cases based on a Gaussian omnidirectional spectrum: one with an initial spreading parameter of $\varsigma_0 = 15°$, denoted as GG15, and another with an initial spreading parameter of $\varsigma_0 = 20°$, denoted as GG20. The comparison is based upon a *mean wavenumber* $\mathcal{K}(t)$ for the spectrum:

$$\mathcal{K} = \frac{\sum_i k_i a(k_i, \theta_i)}{\sum_i a(k_i, \theta_i)}, \tag{3}$$

defined as the ratio of the first spectral moment and the zeroth spectral moment for the amplitude spectrum. Here, the wavenumber, direction and amplitude of each component is denoted by k_i, θ_i and $a(k_i, \theta_i)$ respectively. Figure 3(a) shows the mean wavenumber $\mathcal{K}(t)$ over the course of the simulation for each case, normalised by the initial value $\mathcal{K}_0$, and indicates that simulations performed with a Gaussian omnidirectional spectrum produce an increase in mean wavenumber over the course of the simulation, irrespective of the initial spreading parameter. However, the simulations performed with a JONSWAP spectrum, cases JG15 and JE, indicate a different trend; the mean wavenumber remains approximately constant during the early stages of evolution and reduces during focus. Thus, the increase in mean wavenumber observed for the Gaussian cases, GG15 and GG20, appears to be associated with redevelopment of the initially-absent high-wavenumber tail. Focused wave events with broader bandwidths and high values of directional spreading exhibit a reduced focal time due to linear mechanisms of dispersion. Thus, an increase in directional spreading and inclusion of the high-wavenumber tail may be expected to reduce the nonlinear features of an extreme wave event in an integral sense. However, we have also considered the rates of energy transfer which arise for the wave groups during the steepest stages of evolution. The growth rate calculation is based on the component which initially coincides with the peak of the wavenumber spectrum. The wave action density spectrum has been calculated from the amplitude spectrum [15] and a dimensionless growth rate calculated:

$$\big[\partial \mathcal{A}(k_i, \theta_i)/\partial t\big] T_0 \big/ \mathcal{A}(k_i, \theta_i) = O(\epsilon^2 \omega_0 T_0). \tag{4}$$

based on the wave action density of the component, $\mathcal{A}(k_i, \theta_i)$. Note that the RHS of Eq. (4) is the *dynamic* $O(\epsilon^2 \omega_0 T_0)$ timescale associated with nearly-resonant interactions [16]. The effect of the high-wavenumber tail on the rates of energy transfer is summarised in Fig. 3(b) which shows the maximum growth rate for the spectral peak, observed at any point in the simulation, on the ordinate. The abscissa shows the corresponding spreading parameter (ς), at the time that the maximum growth rate occurs. Directional spreading reduces the maximum growth rate for the Gaussian cases. Cases GG15 and JG15 exemplify the role of the high-wavenumber tail in suppressing rates of energy transfer; the two cases exhibit a similar spreading parameter but the maximum growth rate for case GG15 is a factor of three faster than case JG15. The slower growth rate for case JG15 is particularly unexpected because the JG15 focused wave event is arguably steeper than the GG15 event. The linear steepness has been calculated from $A_L k_p$ which incorporates the

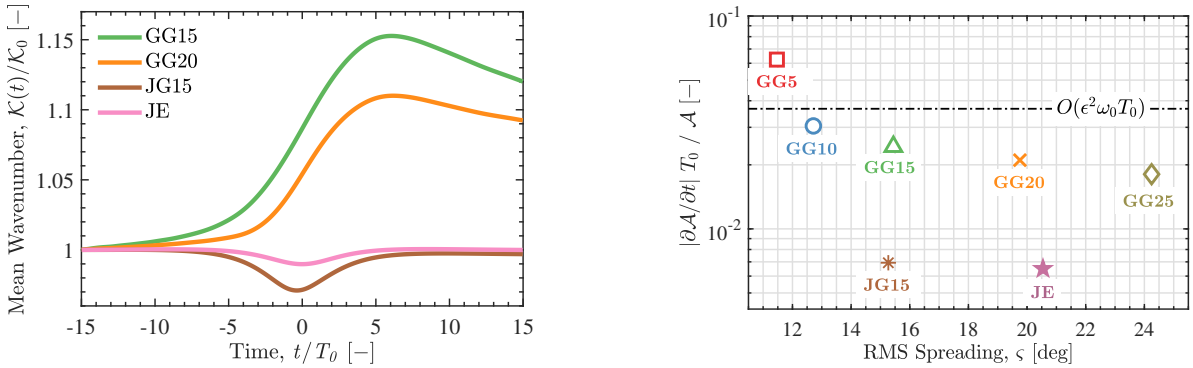

(*a*) (*b*)

Fig. 3. The stabilising effect of directional spreading and the high-wavenumber tail for wave groups with a steepness of $A_L k_p = 0.24$: (*a*) mean wavenumber $\mathcal{K}(t)$ normalised by the initial value $\mathcal{K}_0$ for cases: GG15 (—), GG20 (—), JG15 (—), JE (—). (b) Maximum growth rate for the component initially coinciding with the spectral peak, plotted against the RMS spreading parameter $\varsigma(t)$ at the corresponding time. An estimate of the 'dynamic' growth rate $O(\epsilon^2\omega_0 T_0)$ associated with near-resonant interactions is indicated (— · —).

spectral peak, at the start of the simulation, as the characteristic wavenumber. However, a JONSWAP omnidirectional spectrum features a high-wavenumber tail which should result in a characteristic wavenumber above k_p, suggesting a steeper wave event than indicated by the parameter $A_L k_p$. A proxy for steepness is the number of iterations required at every time step by the GMRES algorithm in *OceanWave3D*. The iteration count has previously been shown to be grid independent when combined with the multi-grid preconditioning scheme we have used in this study. Thus, the finer grid resolution of the JONSWAP cases does not significantly influence the iteration count and we can compare the GMRES iteration count for the Gaussian and JONSWAP cases as an approximate indicator of nonlinearity. Table II lists the average and maximum number of GMRES iterations for each case. The JONSWAP cases, JG15 and JE, both list maximum iteration counts in excess of all the GG cases. However, the maximum growth rate for case GG15 is significantly higher than the maximum growth rate for case JG15. Thus, the high-wavenumber tail, in particular, appears to suppress the rates of energy transfer for the spectral peak. Suppression of the spectral evolution is, thus, not only due to the reduced focal time of broadbanded events. Rather, the rates of energy transfer are also suppressed even at the steepest stages of focusing. Thus, directional spreading and the high-wavenumber tail appear to be integral features of a form of spectral equilibrium which suppress the nonlinear attributes of a steep, focusing wave group.

VI. Engineering Relevance

We show that focused wave events in sea-states without a fully-developed spectral tail are more likely to exhibit attributes of nonlinearity. Certain physical processes are known to suppress the development of the high-wavenumber tail, including wave blocking by currents and energy dissipation by ice sheets, which could influence the characteristics of focused wave events in the immediate vicinity. Furthermore, a Gaussian omnidirectional spectrum is frequently used as a simplified input to simulations / analytical models and our work suggests that redevelopment of the spectral tail could result in exaggerated nonlinearity for individual wave events in such analyses.

References

[1] Trulsen, K., 'Rogue Waves in the Ocean, the Role of Modulational Instability, and Abrupt Changes of Environmental Conditions that Can Provoke Non Equilibrium Wave Dynamics,' In *The Ocean in Motion*, Springer, pp. 239-247, 2018.

[2] Xiao, W., Liu, Y., Wu, G., and Yue, D. K. P., 'Rogue wave occurrence and dynamics by direct simulations of nonlinear wave-field evolution,' J. Fluid Mech., 2013, **720**, pp.357-392.

[3] Dysthe, K. B., Trulsen, K., Krogstad, H., and Socquet-Juglard, H., 'Evolution of a narrow-band spectrum of random surface gravity waves,' J. Fluid Mech., 2003, **478**, pp.1-10.

[4] Fujimoto, W., Waseda, T., and Webb, A., 2018. "Impact of the four-wave quasi-resonance on freak wave shapes in the ocean". *Ocean Dynamics*, DOI: 10.1007/s10236-018-1234-9.

[5] Latheef, M., Swan, C., and Spinneken, J., 2017. "A laboratory study of nonlinear changes in the directionality of extreme seas". *Proc. R. Soc. A*, **473**: 20160290.

[6] Adcock, T.A.A., Taylor, P.H., Draper, S., 2015. "Nonlinear dynamics of wave-groups in random seas: unexpected walls of water in the open ocean". *Proc. R. Soc. A*, **471**: 20150660.

[7] Adcock, T.A.A., and Taylor, P.H., 2016. "Fast and local non-linear evolution of steep wave-groups on deep water: A comparison of approximate models to fully nonlinear simulations". *Phys. Fluids*, **28**: 016601.

[8] Gibbs, R. H., and Taylor, P. H., 'Formation of walls of water in 'fully' nonlinear simulations,' Appl. Ocean Res., 2005, **27**, pp. 142–157.

[9] Engsig-Karup, A. P., Bingham, H.B., and Lindberg, O., 'An efficient flexible-order model for 3D nonlinear water waves,' J. Comp. Phys., 2009, **228**, pp. 2100–2118.

[10] Barratt, D., Bingham, H. B., and Adcock, T. A. A., 'Nonlinear Evolution of a Steep, Focusing Wave Group in Deep Water Simulated With OceanWave3D,' J. Offshore Mech. Arct. Eng., 2020, **142**(2), 021201.

[11] Dalzell, J. F., 'A note on finite depth second-order wave-wave interactions,' Appl. Ocean Res., 1999, **21**, pp. 105–111.

[12] Ewans, K. C., 'Observations of the directional spectrum of fetch-limited waves,' J. Phys. Oceanogr., 1998, **28**, pp. 495–512.

[13] Boccotti, P., 'Some new results on statistical properties of wind waves,' Appl. Ocean Res., 1983, **5**, pp. 134–140.

[14] Stiassnie, M., 'Note on the modified nonlinear Schr odinger equation for deep water waves,' Wave Motion, 1984, **6**(4) pp. 431–433.

[15] Komen, G. J., Cavaleri, L., Donelan, M., Hasselmann, K., Hasselmann, S., and Janssen, P. A. E. M., 'Dynamics and modelling of ocean waves,' Cambridge University Press, 1994.

[16] Stiassnie, M., 'On the strength of weakly nonlinear theory for surface gravity waves,' J. Fluid Mech., 2017, **810**, pp. 1–4.